STATISTICS, OPTIMIZATION AND INFORMATION COMPUTING
Stat., Optim. Inf. Comput., Vol. **10**, September 2022, pp 998–1020.
Published online in International Academic Press (www.IAPress.org)

An Alternative Computation of the Entropy of 1D Signals Based on Geometric Properties†

Cristian Bonini [1], Andrea Rey [2,*], Dino Otero [3], Ariel Amadio [3], Manuel García Blesa [2], Walter Legnani [2]

[1] *Center of Research, Development and Innovation in Electric Energy, Universidad Tecnológica Nacional Facultad Regional General Pacheco, Argentina*
[2] *Center of Signal and Image Processing, Universidad Tecnológica Nacional Facultad Regional Buenos Aires, Argentina*
[3] *Center of Vehicle Research, Development and Innovation, Universidad Tecnológica Nacional Facultad Regional General Pacheco, Argentina*

Abstract The objective of this work is to present a novel methodology based on the computation of a couple of geometric characteristics of the position of the data points in 1D signal to propose an alternative estimation of signal entropy. The conditions to be fulfilled by the signal are minimal; only those necessary to meet the sampling theorem requirement are enough. This work shows some examples in which the proposed methodology can distinguish among signals that cannot be differentiated by other in-use alternatives. Additionally an original example where the usual ordinal pattern algorithm to compute entropy is not applicable, is presented and analyzed. The proposal developed through this work carries some advantages over other alternatives and constitutes a true advancement in the pathway to compute the distribution function of the sequential points of 1D signals later used to compute the entropy of the signal.

Keywords Order Pattern Distribution, Permutation Entropy, Symbolic Dynamics, Signal Entropy, Data Points Geometry

MSC 2020 subject classifications 94A12, 94A17

DOI: 10.19139/soic-2310-5070-1523

1. Introduction

The quest to get an efficient method to compute the entropy of a data series is based upon the estimation of some distribution function of the signal points. In this sense, the Bandt and Pompe [4] proposal is extensively used with real success. In this methodology, the structure and correlation among the data points relies on the symbolic dynamics of an alphabet associated with the sequence of points in the signal. References [14, 3] are examples of books in the literature about ordinal patterns. For a wide sense and combined with symbolic dynamics, *c.f.* [15].

The benefits of the Bandt and Pompe methodology [4] are widely demonstrated, as can be found in works such as [20, 21, 26, 27] and internal references. The analysis of the ordinal pattern selection is discussed in a clear way by [16] as function of its variability. In other order, a review of the ordinal pattern methodology through its twenty year of history was presented in [7], which results a very interesting and useful source of information. In the seeking of recent research, ordinal patterns transitions networks (OPTN) constitute one of the trends as it can be see in [8] and other variants such as [24].

†This work was partly supported by UTN-FRBA grant PID 8120.
*Correspondence to: Andrea Rey (Email: arey@frba.utn.edu.ar). Center of Signal and Image Processing, Universidad Tecnológica Nacional Facultad Regional Buenos Aires. 981 Medrano Avenue, Buenos Aires, Argentina (C1179 AAQ).

ISSN 2310-5070 (online) ISSN 2311-004X (print)

However, there are aspects that demand some caution in its use. In general terms, for example, it cannot be applied to very short data series, it requires the adjustment of two parameters known as the embedding time delay and the embedding dimension or motif, and it does not produce a different result if it is applied to a synthetic signal with linear or exponential growth.

Another inherent problem of the ordinal pattern methodologies in use, is the correct identification and counting of the missing or forbidden patterns. To solve this issue, some ingenious solutions have been proposed, which can be seen for example in [11] and [9], which overcome some of the drawbacks of this problem, but in no case resolve it completely.

In this work, a novel methodology based on the strictly geometric aspects of the 1D signal or data series is employed to redefine the way to construct the pattern counter for the distribution function of the data points later used to calculate entropy.

It should be notice that this proposal can be applied to signals whose length cannot be analyzed using the Bandt and Pompe methodology [4]. In addition, it does not require the fine tuning of any parameter and does not make any assumptions about the distribution function of the data points coming from the signal nor about the nature of the system that generates the signal. The problem of the missing or forbidden patterns does not appear since only the present points of the data series are taken into account for the computation of the present approach.

Summing up, the requirements of this proposal are practically none, the only assumption that is necessary to be satisfied is to fulfill the conditions of the sample theorem. Then, the methodology of the present work, which is based on the geometric locations of the data points, can be applied to any good sampled signal.

To characterize the geometric structure of the signal, two new variables are introduced, named *delta moment* and *delta state*, denoted by ΔM and ΔS respectively, and with these new variables a transformation from the 1D signal to the 2D space of the patterns counter is defined.

The proposed new algorithm is sensible to noise and can be used to characterize incremental noise when it is proportional to the signal amplitude.

The capacity of differentiation among several kinds of growing synthetic signals, which most of the current methodologies do not differentiate, together with the ability to register particularities in the pattern distribution of the chaotic and stochastic signals, suggests many potential uses of the present algorithm. In such a way, this result encourages the use of the proposal contained in this work to be tested in many fields of 1D signals and time series processing.

This work is organized as follows. Section 1 presents the introduction and motivation. The new geometric pattern transformation (GPT) algorithm is introduced in Section 2, where the innovation in the pattern counting is developed. Section 3 is devoted to show some applications, among them: synthetic signals to expose how the new proposal can differentiate signals whose distribution patterns are undistinguished by other methodologies. In Section 4, examples of chaotic and stochastic signals are presented to point out how the new methodology can differentiate these group. An application to nuclear decay of the rotational states of deformed nuclei known as the "back bending decay" is developed in Section 5 to show the advantage of using of the new scheme in case of short data series. In Section 6, based on the GPT, a vector of entropy is computed to estimate the entropy of a given signal whose coordinates correspond to the entropy of each pattern. Finally, Section 7 contains the conclusions of the current proposal.

This work can be considered as an extension of the ordinal pattern methods to estimate the entropy of a 1D signal in such a way that the principal characteristics of the present proposal can be highlighted as follows:

- The main advantage of the GPT is to transform a 1D series (signal or time series) to a plane which retrieves structural details of the data points that constitutes the original series.
- It can be applied to very short length signals, that other methodologies of analysis are forbidden to be used.
- It can be used both in signals sampled at constant intervals and those sampled at irregular intervals, since the interval between samples is not used at any time for the calculation of the new GPT variables.
- It does not require the fine tunning of any parameter, like the embedding dimension or the embedding time delay employed for the computation of the permutation entropy.
- It is low computational demand since the GPT is a linear transformation that assigns to every three consecutive data points in the signal, a pair in the $\Delta M \times \Delta S$ plane.

- It is possible to distinguish among chaotic, stochastic and analytic signals.
- The problem of missing or forbidden patterns to compute the entropy, typically affecting the ordinal pattern methods, is not present in the GPT algorithm since only the actual points of the signal are considered for the computations.
- The vectorized form of the entropy obtained from the GPT can distinguish different types of colored noises without having to transform the signal in the Fourier frequency domain.
- Every coordinate of the vector retrieves the entropy associated at a certain pattern in the $\Delta M \times \Delta S$ plane.

2. Geometric Pattern Transformation (GPT)

In this section we develop a new proposal named Geometric Pattern Transformation, with the aim to qualify and quantify different structures that belong to the same permutation pattern given by the ordinal pattern methods. This analysis is inspired by the fact that permutation patterns distribution is not sensitive to tiny variations of a given sequence. Basically, this transformation when applied to one-dimensional series produces a cloud of points in a two-dimensional space. Moreover, ordinal patterns define regions in this plane which can be used to establish the behavior of the series within each area. The distribution of these points allows to extract more information from the series, even when the number of values recorded in the signal is scarce.

Given a signal with values $\{y_n\}$, recall that for an embedding number $m = 3$ and time delay $\tau = 1$, the permutation patterns are represented as shown in Figure 1.

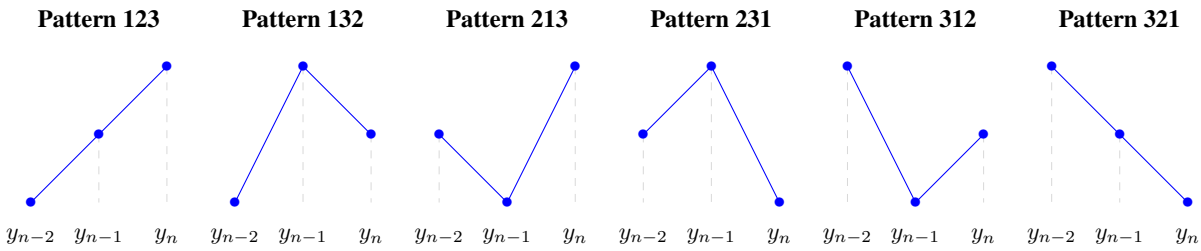

Figure 1. Permutation patterns for $m = 3$ and $\tau = 1$.

A natural question is whether different signal shapes from the same permutation pattern can be distinguished through geometry conditions (see Figure 2). In an attempt to answer this query, a GPT is defined in the lines below.

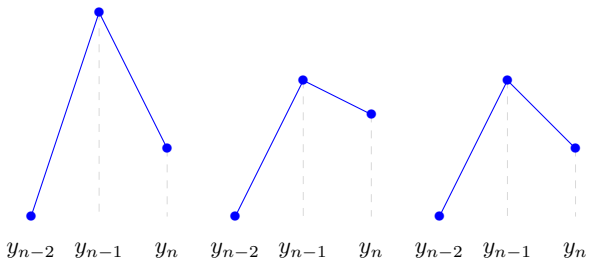

Figure 2. Different signal shapes sharing the same pattern 132.

For a given signal, partitions of length three are considered. Let y_{n-2}, y_{n-1}, y_n be one of such partitions. The corresponding state variation is defined by

$$\Delta S = (y_{n-1} - y_{n-2}) + (y_n - y_{n-1}) = y_n - y_{n-2}. \tag{1}$$

Moreover, the corresponding moment variation is defined by

$$\Delta M = (y_{n-1} - y_{n-2}) + 2(y_n - y_{n-1}) = 2y_n - y_{n-1} - y_{n-2}. \tag{2}$$

Using this two measures of variation, the pair $(\Delta M, \Delta S)$ can be associated to each partition (y_{n-2}, y_{n-1}, y_n). In a general context, it is deduced the existence of a linear transformation $T_{MS} : \mathbb{R}^3 \to \Delta M \times \Delta S$ given by

$$T_{MS}(x, y, z) = (2z - y - x, z - x). \tag{3}$$

Consider the following change of variables:

$$\begin{cases} t_1 &= y - x, \\ t_2 &= z - y, \end{cases} \tag{4}$$

from which it can be noticed that $t_1 + 2t_2 = 2z - y - x$ and $t_1 + t_2 = z - x$. Thus, an element in the image of T_{MS} can be written as:

$$T_{MS}(x, y, z) = (t_1 + 2t_2, t_1 + t_2) = t_1(1, 1) + t_2(2, 1). \tag{5}$$

Let $v_1 = (1, 1)$ and $v_2 = (2, 1)$. Since they are linearly independent, it has been proved that $B = \{v_1, v_2\}$ is a basis of the image of T_{MS}. The basis change from canonic basis E to B produces a new axis system, which is represented in blue in Figure 3a. Let $[P]_E$ and $[P]_B$ denote the coordinates of the point P in the basis E and B, respectively. If P belongs to the horizontal axis,

$$[P]_E = (x, 0) \Longrightarrow P = (x, 0) = -x(1, 1) + x(2, 1) \Longrightarrow [P]_B = (-x, x). \tag{6}$$

In other words, if $[P]_B = (t_1, t_2)$ and P is a point in the horizontal axis, then $t_2 = -t_1$. Thus, the line r, which is plotted in red, has equation $t_2 = -t_1$.

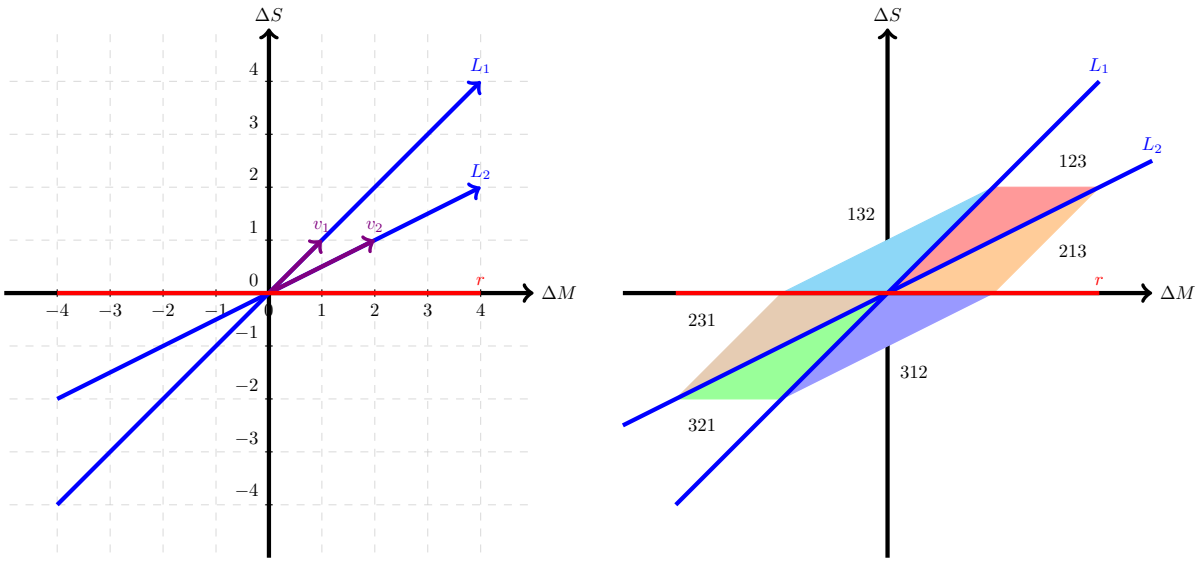

(a) New coordinate system.

(b) Regions occupied by the permutation patterns, where the extension of the regions are merely illustrative.

Figure 3. Regions in the $\Delta M \times \Delta S$ plane in terms of T_{MS}.

The possible outcomes of T_{MS} in terms of permutation patterns can be analyzed as follows. The coordinate systems defined by L_1 and L_2, respectively generated by v_1 and v_2, and line r split the $\Delta M \times \Delta S$ plane into six regions, where the patterns are located as can be seen in Figure 3b. It is immediate to derive a clockwise order for the ordinal patterns: 123, 132, 231, 321, 312 and 213. Notice the reflection symmetry of the pairwise patterns 123-321, 132-312 and 231-213. The patterns fit into the following well-defined two-dimensional zones.

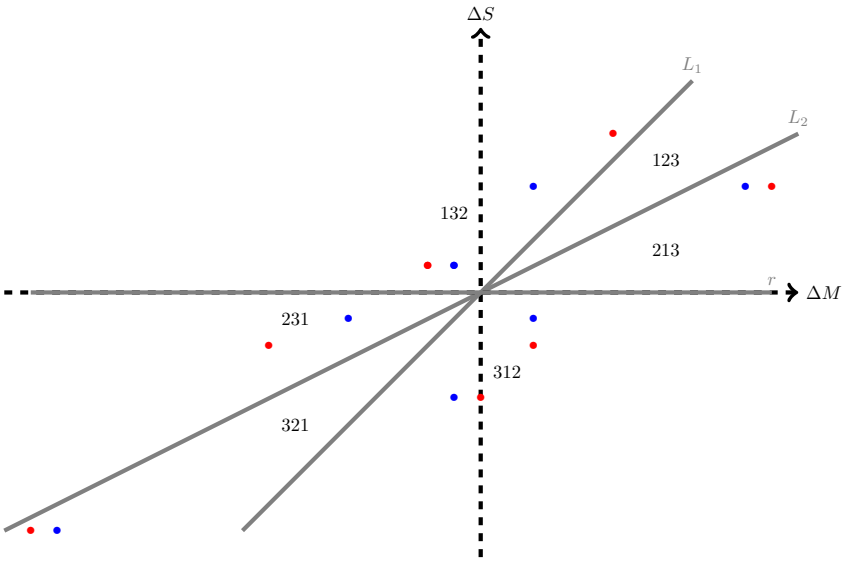

Figure 4. Example of GPT applied to signal S_1 (red) and S_2 (blue).

- Pattern 123: $y_{n-2} < y_{n-1} < y_n \Longrightarrow t_1 > 0 \wedge t_2 > 0 \wedge t_2 > -t_1$.
- Pattern 132: $y_{n-2} < y_n < y_{n-1} \Longrightarrow t_1 > 0 \wedge t_2 < 0 \wedge t_2 > -t_1$.
- Pattern 231: $y_{n-1} < y_n < y_{n-2} \Longrightarrow t_1 > 0 \wedge t_2 < 0 \wedge t_2 < -t_1$.
- Pattern 321: $y_n < y_{n-1} < y_{n-2} \Longrightarrow t_1 < 0 \wedge t_2 < 0 \wedge t_2 < -t_1$.
- Pattern 312: $y_n < y_{n-2} < y_{n-1} \Longrightarrow t_1 < 0 \wedge t_2 > 0 \wedge t_2 < -t_1$.
- Pattern 213: $y_{n-1} < y_{n-2} < y_n \Longrightarrow t_1 < 0 \wedge t_2 > 0 \wedge t_2 > -t_1$.

With the aim to illustrate this proposal, a simple example is considered. Let $S_1 = \{3, 7, 1, 5, 2, 9, 8, 0, 4, 1\}$ and $S_2 = \{3, 6, 2, 5, 3, 9, 7, 0, 3, 1\}$ be two signals. The points obtained after applying the GPT to both signals are $\text{GPT}(S_1) = \{(-8, -2), (2, -2), (-2, 1), (11, 4), (5, 6), (-17, -9), (0, -4), (-2, 1)\}$ and $\text{GPT}(S_2) = \{(-5, -1), (2, -1), (-1, 1), (10, 4), (2, 4), (-16, -9), (-1, -4), (-1, 1)\}$. On the other hand, the ordinal patterns with an embedding dimension equal to 3 for both signals are: 231, 312, 132, 213, 132, 321, 312 and 132, implying the same Bandt and Pompe permutation entropy, which is equal to 0.833915. When these signals seem to be indistinguishable using permutation entropy, it can be seen in Figure 4 that the distance from GPT points to the coordinate origin varies strongly for patterns 132 and 231, motivating the analysis of our proposal.

Notice that the transformation given by (3) can be easily generalized as $T_{MS} : \mathbb{R}^n \to \Delta M \times \Delta S$ defined by

$$T_{MS}(y_1, y_2, \ldots, y_n) = \begin{pmatrix} -1 & -1 & \cdots & -1 & n-1 \\ -1 & 0 & \cdots & 0 & 1 \end{pmatrix} \begin{pmatrix} y_1 & y_2 & \cdots & y_n \end{pmatrix}^t, \tag{7}$$

where x^t indicates the transpose of x.

3. GPT applied to continuous functions

In this section, the result of GPT is investigated when this transformation is applied to several simple and well known cases. Let $y = f(x)$ be a continuos function, which can be approximated by the Taylor polynomial of first degree centered in $x = x_0$ as follows:

$$f(x) \cong f(x_0) + f'(x_0)(x - x_0), \tag{8}$$

where f' denotes the derivative respect to variable x and the error is given by $0.5f''(\xi)(x - x_0)^2$ for a given ξ in the interval defined by x and x_0.

The following notation is used: $y_n = f(x_n)$ and $y'_n = f'(x_n)$. Given y_{n-2}, y_{n-1}, y_n; three consecutive values in the signal, the step between two observations can be seen as $p = x_n - x_{n-1} = x_{n-1} - x_{n-2}$. If p is sufficiently small and using (8) with $x_0 = x_n$, it holds that:

$$y_{n-1} = f(x_{n-1}) \cong f(x_n) - pf'(x_n) = y_n - py'_n, \tag{9}$$

$$y_{n-2} = f(x_{n-2}) \cong f(x_n) - 2pf'(x_n) = y_n - 2py'_n. \tag{10}$$

The corresponding points in the $\Delta M \times \Delta S$ plane, after applying the GPT, can be expressed as:

$$[\Delta M, \Delta S] = [2y_n - y_{n-1} - y_{n-2}, y_n - y_{n-2}]. \tag{11}$$

Thus, replacing by (9) and (10) into (11),

$$[\Delta M, \Delta S] \cong [2y_n - y_n + py'_n - y_n + 2py'_n, y_n - y_n + 2py'_n] = [3py'_n, 2py'_n]. \tag{12}$$

From (12), it is clear that

$$\Delta S \cong \frac{2}{3}\Delta M. \tag{13}$$

It is worth noticing that the goodness of the linear fitting depends of the values of the second derivative of the involved signal.

With the aim to investigate the results of applying the GPT on well known continuous functions, the following cases are considered.

- **Linear function.** For line $y = ax + b$, the single point $[3ap, 2ap]$ is obtained, where p is the step from which the line is constructed.
- **Quadratic function.** Given $y = ax^2 + bx + c$, the line of equation $\Delta S = 2(\Delta M - ap^2)/3$ is obtained.
- **Polynomial function of cubic degree.** If $y = ax^3 + bx^2 + cx + d$ and p is sufficiently small, the line given by the expression $\Delta S \cong 2(\Delta M - 3ap^3 - bp^2)/3$ is reached.
- **Rational function.** Given $y = 1/x^n$ $(n = 1, 2, 3)$, the results of applying the linear model to the points $[\Delta M, \Delta S]$ for $x \in [1, 100]$, with Pearson coefficient $R = 1$, are shown in Table 1.
- **Logarithmic function.** For $\log_b(x)$ $(b = 0.5, e, 10)$ and $x \in [1, 100]$, the linear relation between ΔM and ΔS with $R = 1$ is described in Table 2.
- **Exponential function.** For e^x and e^{-x}, it is easy to obtain the relation $\Delta S \cong 2\Delta M/3$ for $p < 0.1$.

As a conclusion, based on the evidences shown, the application of GPT to continuous functions seems to generate a polynomial where the linear term predominates with a value close to $2/3$, although it varies slightly with the p size. Thus, this step could be a very important ingredient in the distribution of the points in the $\Delta M \times \Delta S$ plane.

In order to analyze the signal to noise ratio, two experiments were performed. In one of them, the signal is contaminated with noise proportional to its amplitude. In the other case, the noise level is of constant intensity. In particular, the GPT is very sensitive to the presence of noise, as it can be seen as follows. An interesting example corresponds to a straight line embedded in a proportional noise to 0.005 of the signal amplitude. Although the straight line is slightly contaminated, the GPT scatter plot shows a large dispersion (see Figure 5b). Figure 6a shows the case of a contaminated quadratic parabola in the same way as the previous case. Notice that a small disturbance in the parabola appears to be strongly amplified in the GPT, as it is shown in Figure 6b. The dispersion in the cloud of points is originated for high values in the parabola and some of them may even be located in the left bottom corner of the GPT scatter plot. This is a point that must be considered when studying GPT scatter plots, *i.e.* how the type of noise may affect the signal.

Table 1. Lineal regression of the GPT applied to $f(x) = 1/x^n$ $(n = 1, 2, 3)$.

Function	p	Relation
$\frac{1}{x}$	10	$\Delta S = 0.9602\Delta M + 0.0043$
	1	$\Delta S = 0.7892\Delta M + 0.0008$
	0.1	$\Delta S = 0.6830\Delta M$
	0.01	$\Delta S = 0.6683\Delta M$
	0.001	$\Delta S = 0.6668\Delta M$
$\frac{1}{x^2}$	10	$\Delta S = 0.9602\Delta M + 0.0086$
	1	$\Delta S = 0.7892\Delta M + 0.0015$
	0.1	$\Delta S = 0.6830\Delta M$
	0.01	$\Delta S = 0.6683\Delta M$
	0.001	$\Delta S = 0.6668\Delta M$
$\frac{1}{x^3}$	10	$\Delta S = 0.9602\Delta M + 0.0128$
	1	$\Delta S = 0.7892\Delta M + 0.0023$
	0.1	$\Delta S = 0.6830\Delta M$
	0.01	$\Delta S = 0.6683\Delta M$
	0.001	$\Delta S = 0.6668\Delta M$

Table 2. Lineal regression of the GPT applied to $f(x) = \log_b(x)$ $(b = 0.5, e, 10)$.

Function	p	Relation
$\log(x)$	10	$\Delta S = 0.8428\Delta M - 0.0411$
	1	$\Delta S = 0.7147\Delta M - 0.0016$
	0.1	$\Delta S = 0.6729\Delta M$
	0.01	$\Delta S = 0.6673\Delta M$
	0.001	$\Delta S = 0.6667\Delta M$
$\ln(x)$	10	$\Delta S = 0.8428\Delta M - 0.0947$
	1	$\Delta S = 0.7147\Delta M - 0.0038$
	0.1	$\Delta S = 0.6729\Delta M - 0.0001$
	0.01	$\Delta S = 0.6673\Delta M$
	0.001	$\Delta S = 0.6667\Delta M$
$\log_{1/2}(x)$	10	$\Delta S = 0.8428\Delta M + 0.1366$
	1	$\Delta S = 0.7147\Delta M + 0.0054$
	0.1	$\Delta S = 0.6729\Delta M + 0.0001$
	0.01	$\Delta S = 0.6673\Delta M$
	0.001	$\Delta S = 0.6667\Delta M$

4. GPT applied to chaotic and stochastic signals

This section presents some examples in which the results of the GPT applied to different dynamical behaviors are shown.

- **Random uniform set.** Applying the transformation to a uniform pseudo-random set, we obtain the scatter plot shown in Figure 8 (left). Even though the GPT plot does not have its origin in random numbers, the extreme values of the interval $[0, b]$ determine the hexagon in which the scatter plot is developed. Then, the GPT is determined in a space delimited by this hexagon, dependent on the expressed values of the original signal. The lines that separate the patterns can be determined very easily as follows. In

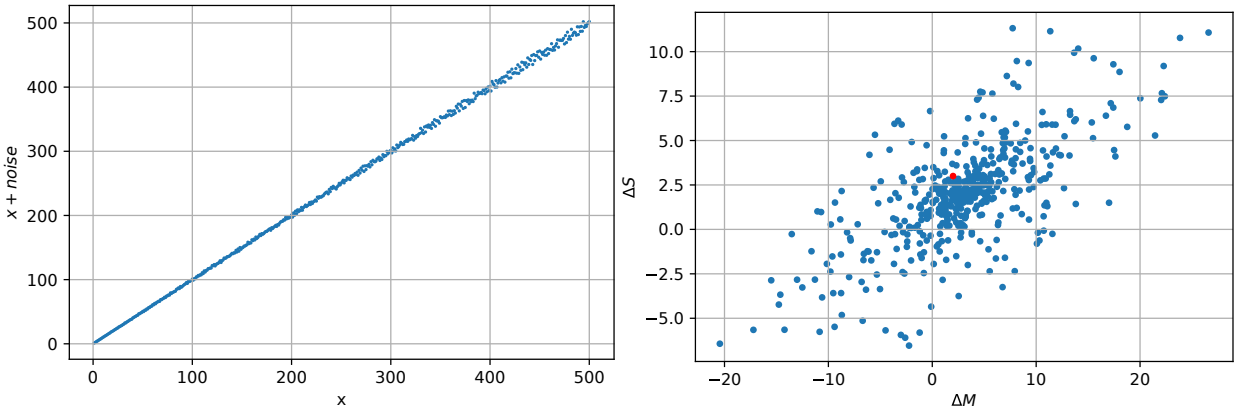

(a) Straight line contaminated with proportional uniform random noise of level 0.005.

(b) Plot of the GPT applied to the noised curve on the left (scatter plot in blue) and to its noiseless version (red point $(2, 3)$).

Figure 5. Effect of the GPT application to noised linear signal.

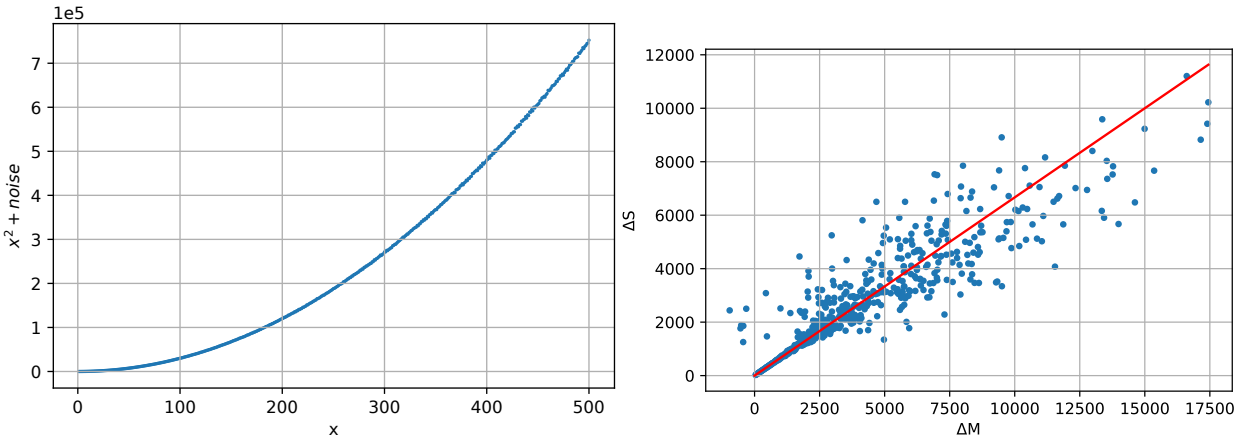

(a) Quadratic increasing signal contaminated with a proportional uniform random noise of 0.005 level.

(b) Plot of the GPT applied to the noised curve on the left (scatter plot in blue) and to its noiseless version (red line of slope $2/3$).

Figure 6. Effect of the GPT application to noised quadratic signal.

order to study the regions occupied by the GPT applied to the random uniform signal in the interval $[0, b]$, the points $V_1 = (2b, b)$, $V_2 = (b, b)$, $V_3 = (-b, 0)$, $V_4 = (-2b, -b)$, $V_5 = (-b, -b)$ and $V_6 = (b, 0)$ are considered. Moreover, if r_{ij} denotes the line that passes through V_i and V_j it can be seen that $r_{12} : y = b$, $r_{23} : y = (x + b)/2$, $r_{34} : y = x + b$, $r_{45} : y = -b$, $r_{56} : y = (x - b)/2$ and $r_{61} : y = x - b$. It is going to be proved that the boundaries of these regions are precisely these lines. Notice first that if $x, y \in [0, b]$, then $-b \leq x - y \leq b$. Notice that in this proof, the range of signal values -which are non-negative- is considered to define the vertices instead of the range of GPT points.

– Region of the pattern 213 where $y_{n-1} < y_{n-2} < y_n$:

$$\begin{cases} \Delta S > 0, \\ \Delta M - b \leq \Delta S < \Delta M/2, \end{cases}$$

where the left hand side of the second condition holds since

$$\begin{aligned} y_{n-1} - y_n &\geq -b, \\ y_n - y_{n-2} &\geq 2y_n - y_{n-1} - y_{n-2} - b, \\ \Delta S &\geq \Delta M - b. \end{aligned}$$

– Region of the pattern 123 where $y_{n-2} < y_{n-1} < y_n$:

$$\begin{cases} \Delta M/2 < \Delta S < \Delta M, \\ \Delta S \leq b, \end{cases}$$

$\Delta M/2 < \Delta S < \Delta M$ and $\Delta S \leq b$, where the second condition holds since $\Delta S = y_n - y_{n-2} \leq b$.

– Region of the pattern 132 where $y_{n-2} < y_n < y_{n-1}$:

$$\begin{cases} \Delta S > 0, \\ \Delta M < \Delta S \leq (\Delta M + b)/2, \end{cases}$$

$\Delta S > 0$ and $\Delta M < \Delta S \leq (\Delta M + b)/2$, where the right hand side of the second condition holds since

$$\begin{aligned} y_{n-1} - y_{n-2} &\leq b, \\ 2(y_n - y_{n-2}) &\leq 2y_n - y_{n-1} - y_{n-2} + b, \\ 2\Delta S &\leq \Delta M + b. \end{aligned}$$

– Region of the pattern 231 where $y_{n-1} < y_n < y_{n-2}$:

$$\begin{cases} \Delta S < 0, \\ \Delta M/2 < \Delta S \leq \Delta M + b, \end{cases}$$

where the right hand side of the second condition holds since

$$\begin{aligned} b &\geq y_{n-1} - y_n, \\ 2y_n - y_{n-1} - y_{n-2} + b &\geq y_n - y_{n-2}, \\ \Delta M + b &\geq \Delta S. \end{aligned}$$

– Region of the pattern 321 where $y_n < y_{n-1} < y_{n-2}$:

$$\begin{cases} \Delta M < \Delta S < \Delta M/2, \\ \Delta S \geq -b, \end{cases}$$

where the last condition holds since $\Delta S = y_n - y_{n-2} \geq -b$.

– Region of the pattern 312 where $y_n < y_{n-2} < y_{n-1}$:

$$\begin{cases} \Delta S < 0, \\ (\Delta M - b)/2 \leq \Delta S < \Delta M, \end{cases}$$

where the left hand side of the second condition holds since

$$\begin{aligned} -b &\leq y_{n-1} - y_{n-2}, \\ 2y_n - y_{n-1} - y_{n-2} - b &\leq 2(y_n - y_{n-2}), \\ \Delta M - b &\leq 2\Delta S. \end{aligned}$$

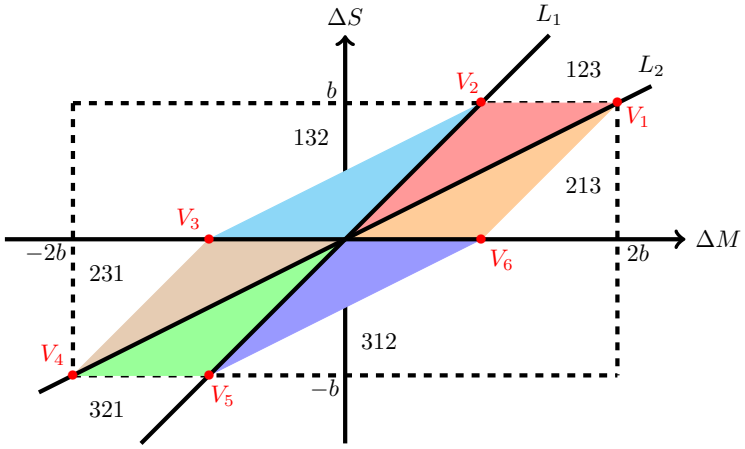

Figure 7. Hexagon defined by the GPT applied to a random uniform signal in the interval $[0, b]$.

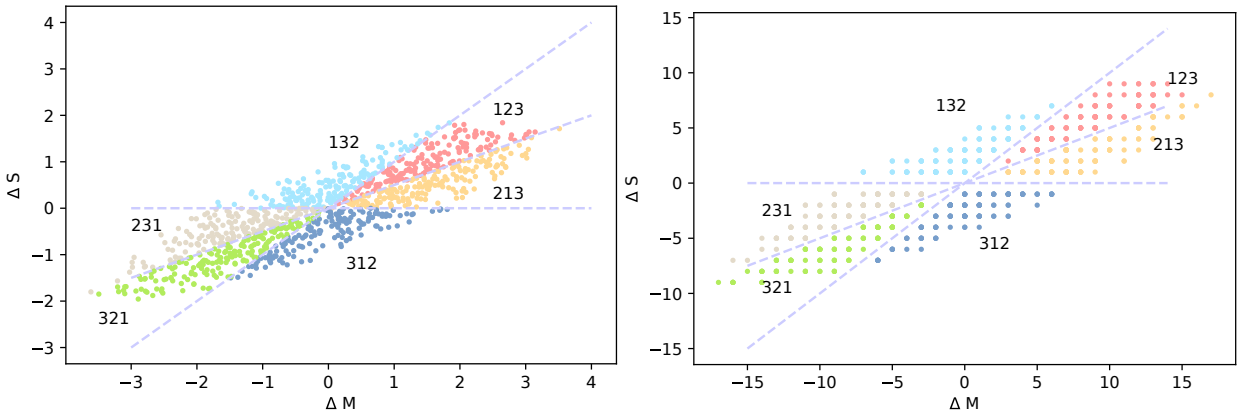

Figure 8. Application of GPT to a uniform pseudo-random signal of length 1000 (left) and to the signal formed by the first 1000 digits of $\sqrt{2}$ (right).

Now the area of each pattern is completely determined as the area of the corresponding triangle. The GPT plot configures a set of points that generate figures in each pattern. Then the GPT configuration space is the one shown in Figure 7.

- **Chaotic Dynamic Equations.** An interesting point is the application over chaotic systems such as the logistic equation. Considering the special value for chaotic region $\lambda = 3.9$, the GPT is applied to the following logistic equation:

$$y_{i+1} = \lambda y_i(1 - y_i). \tag{14}$$

Inside the chaotic region (see Figure 9), the colored graph of patterns depicts a curve whose behavior is like that of an attractor. At the same time, we note that the attractor often has only five colors in chaotic periods. The absence of a particular pattern in the chaotic zones can be observed in Figure 10, in particular pattern 321 within the proposed scheme for an embedding dimension $m = 3$. It is possible to confirm this absence by counting the patterns and coloring each one. This feature was also described in [25]. From another point of view, if λ is considered in the range $[3.7, 4.0]$, the pattern counting is shown in Figure 11. In particular, it can be seen how the counting of pattern 321 (in light green) is always very close to 0. Figure 11 middle and bottom show the results of the bifurcation diagram of the logistic equation and the Lyapunov exponent,

respectively. It is worth noticing that the locations of the main windows of the ordered behaviour agree with the lowest pattern counting presented in Figure 11 (top).

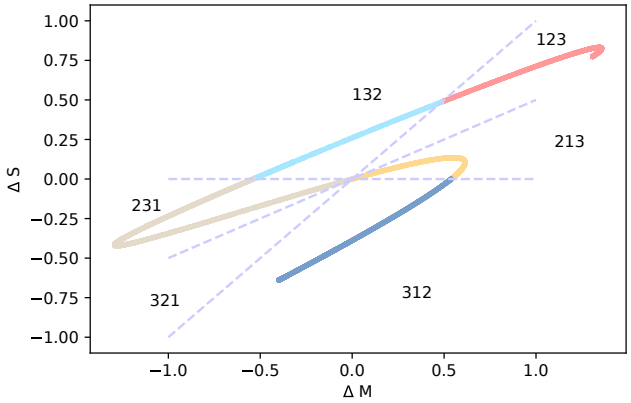

Figure 9. Application of GPT to the logistic equation with $\lambda = 3.9$. Colors indicate every pattern as follows from Figure 3b.

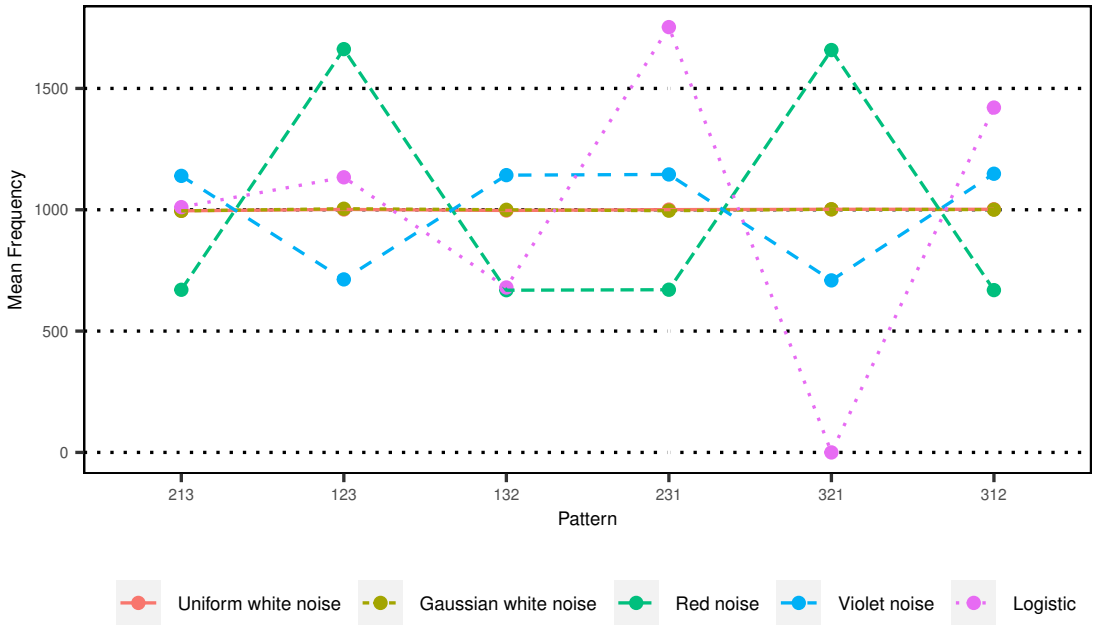

Figure 10. Mean pattern counting over 100 signals with different types of noise and the logistic equation with $\lambda \in [3.90, 3.91]$.

- **Discrete series.** This section is devoted to some special discrete series. The first case to be analyzed is the squared root of two. The begining of the corresponding numeric sequence is:

$$1-4-1-4-2-1-3-5-6-2-3-7-3-0-9-5-0-4-8-8-\cdots$$

The result of the application of the GPT to this numeric series can be seen in Figure 8 (right). The GPT of every data point rotates around line $\Delta S = 0.5000\Delta M + 0.0015$ with a low correlation factor, $R = 0.8661$. The values of the coefficients of the line and the correlation factor vary slightly with the number of digits considered.

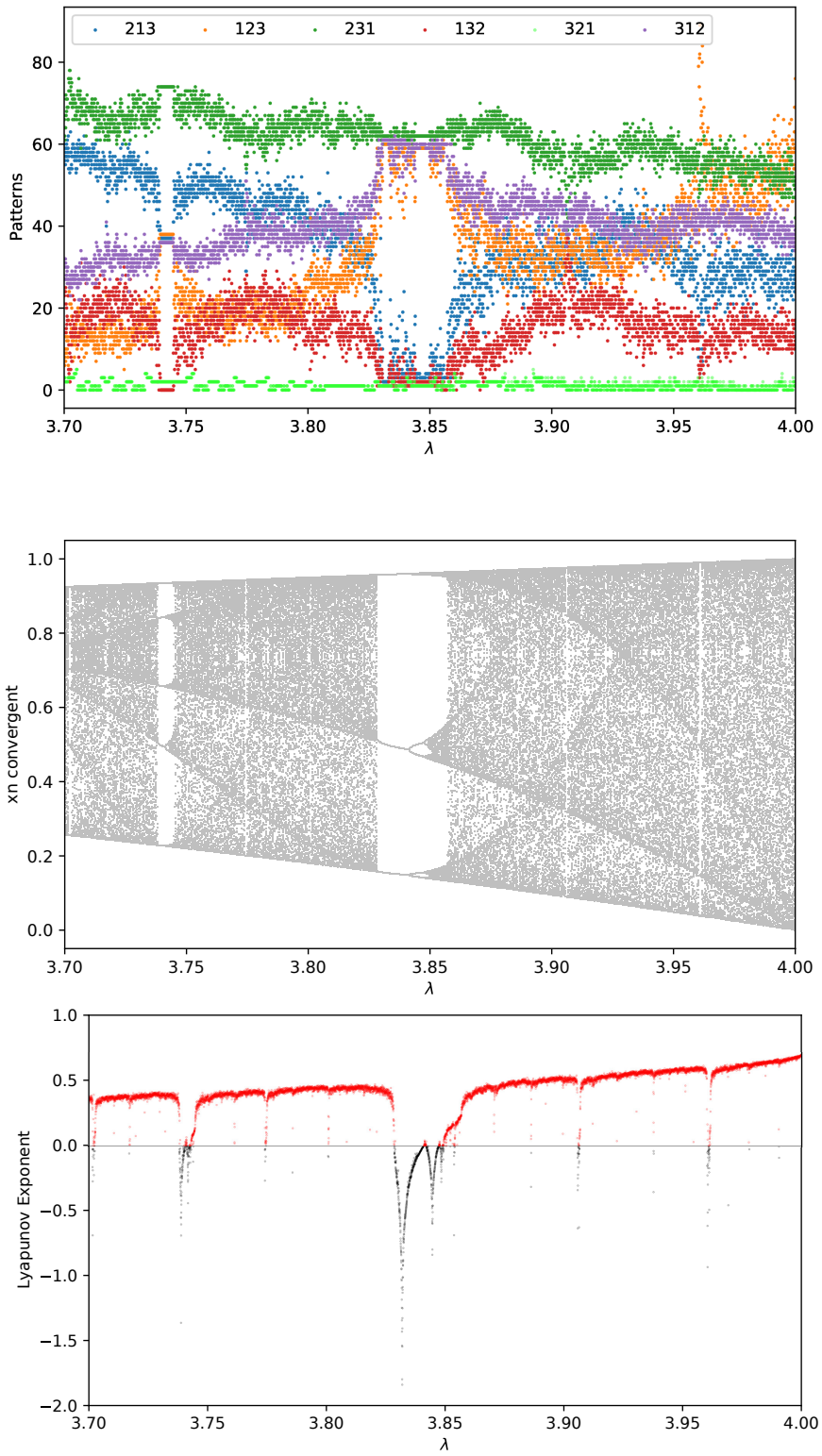

Figure 11. For λ values from 3.70 to 4.00 and a step of 10^{-4} pattern counting of the logistic function (top), bifurcation diagram (middle) and Lyapunov exponent (bottom).

A similar result is obtained with the roots of 3, 5, 6 and 7. Another example selected to show the result of the GPT is the well known golden number $(1+\sqrt{5})/2$. Considered as a number system with an irrational base [5, 23], we obtain $\Delta S = 0.5044\Delta M + 0.0010$ with $R = 1$.
Nothing special is observed for other irrational numbers, such as π for which $\Delta S = 0.4946\Delta M + 0.0031$ ($R = 0.8613$) and e where $\Delta S = 0.4954\Delta M + 0.0005$ ($R = 0.8619$).
A similar result is obtained with the first 1000 prime numbers: $\Delta S = 0.5922\Delta M + 1.7671$, $R = 0.8808$.
Another discrete series is the Fibonacci sequence: $\Delta S = 0.6180\Delta M + \beta$ ($R = 1$), where β depends on the number of data points of the signal analyzed, and $\beta \to 0$ when this number increases.

- **Coloured noises.** To analyze the results of the GPT applied to colored noises, four different types of noises according to their frequency spectrum were used: white Gaussian distributed, white uniform distributed, red and violet noises. All of them were signals of 6000 data points generated according to [28]. The results of the computation of the GPT are shown in Figure 10. The GPT corresponding to the white Gaussian and uniform noises gave practically overlapping results, while for the red and violet noises the GPT results were counter-phase, *i.e.* when one is maximum the other is minimum and *vice versa*. Even when one shows a positive plateau, the other one shows a negative plateau. This is a striking result because, although the different types of noise can be perfectly characterized by a traditional frequency analysis, with the proposed methodology where only a calculation based on the geometry of the signal in the time domain is made, indications of different frequency structures could be obtained without taking into account the frequency domain. Comparing the GPT of the four noises with the logistic map for the coefficient equal to 4, *i.e.* in the range well defined as chaotic, it can be observed that the result of the GPT is different. This fact seems to give evidence that the proposed geometrical transformation would differentiate the behavior of a sensitive chaotic system from the different types of stochastic signals.

5. GPT applied to a very short signal: an example of quantum mechanics

This section analyzes the utility of applying GPT to a short length signal. In general, signals have an electromagnetic origin. The gamma radiation, emitted by excited atoms, molecules, and nuclei, when decaying to the ground state, is also an electromagnetic signal. It is well known that energy levels in quantum systems are discretely distributed in bound systems. Consequently the emitted radiation of energy is also quantified. Then, when decay from a high energy level occurs, a radiation cascade with discrete values is usually generated. In the following paragraphs, an application to nuclear decay originated in the rotation of the nucleus, called Back Bending [22], is described. First, the simple case of the rotational states of a deformed nucleus will be analyzed. In this case, the cascade is easily identifiable and the result obtained is very simple. Rotational energy levels E_J obey the following expression [13]:

$$E_J = \left(\frac{h}{2\pi}\right)^2 \frac{J(J+1)}{2I},\ J = 0, 2, 4, \cdots \tag{15}$$

where h is the Planck constant, J the quantum number corresponding to the angular momentum of the nucleus and I the moment of inertia of the nucleus. The time series that can be analyzed using GPT arises from the transition between the excited states corresponding to the expression (15). There are two possibilities: to analyze the theoretical series given by (15) or the gamma cascade observed experimentally. In the first case, the moment of inertia is assumed constant and the case is named as rigid rotator. In the second case, it will be shown that, when the nucleus rotates, its shape changes and therefore the moment of inertia changes according to the amount of angular momentum it possesses. For the rigid rotator, the relation $J(J+1)$ generates a very simple series for E_J, the energy levels through which the rotation will pass,

$$E_J \approx \{0, 6, 20, 42, 72, 110, 156, 210, 272, 342, 420, 506, 600, 702, 812, 930, 1056\}. \tag{16}$$

The energy jumps, that is, the energy of the gamma rays will be proportional to

$$\Delta E_J = E_\gamma \approx 4J - 2. \tag{17}$$

Applying the GPT to the series given by (17), the point $(-16, -24)$ in the plane ΔM x ΔS is obtained. The coordinates of this point in the energy diagram depend on the real values of E_2. It is important to note that if the energy of the first excited state is taken as given by E_2, the energies of the higher levels follow from (17) as [13],

$$E_J = \frac{1}{6} J(J+1)E_2 \tag{18}$$

However, the experimental observation generated by (18) gives lower values for transitions than theoretically predicted. The deviation can be explained by a centrifugal stretching of the nucleus, in such a way that taking stretching into account, the ratios observed can be explained [12, 17, 2]. Let's first look at the behaviour of the ^{170}Hf gamma emission. This nucleus clearly presents the stretching of the moment of inertia. In Figure 12, the behaviours of the gamma emission for the theoretical case of a rigid rotator and the one observed experimentally are presented. This is a time series emitted with a time interval between 10^{-7} and 10^{-11} seconds, approximately [18].

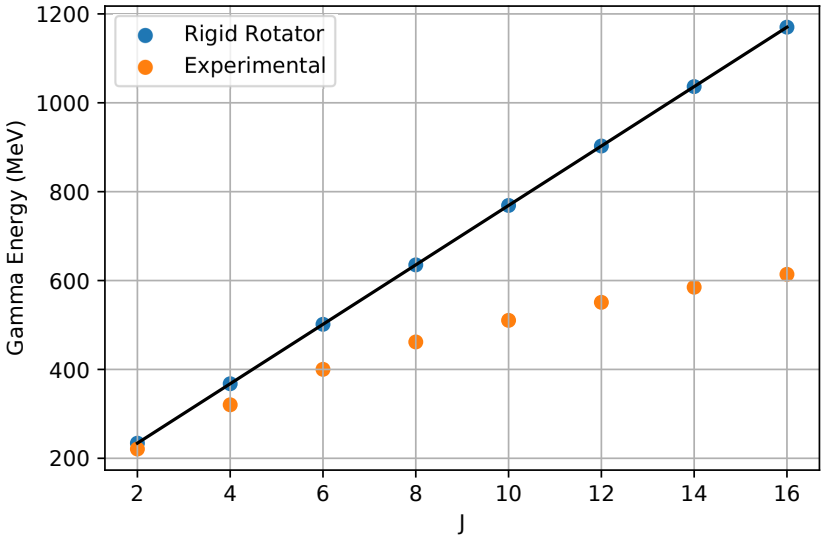

Figure 12. The effect of stretching the moment of inertia deforms the straight line of the theoretical rigid rotator for ^{170}Hf but there is no evidence of Back Bending decay.

Figure 13 shows the evolution of angular momentum using GPT. The rigid rotator locus corresponds to a point, while the experimental values fall almost on a straight line.

Now, the ^{158}Er will be analyzed. This element is considered a classic nucleus since it exhibits two well known Back Bendings as it evolves with increasing angular momentum. Two effects overlap, the stretching and a sharp and strong deformation for $J = 12$ and $J = 26$.

Figure 14 shows the evolution of the angular momentum as a function of the rotational energy in the usual representation. The first Back Bending is located for $J = 12$, and the second one is placed for $J = 26$. Figure 15 shows the evolution of angular momentum using GPT. The emergence of two Back Bendings at $J = 12$ and $J = 26$ and the GPT corresponding to the experimental and theoretical data of the rigid rotator can be observed. The theoretical nuclear aspects are discussed in the literature [1, 6]. GPT representation proves to be a powerful tool for visualizing quantum cascades. In particular, the Back Bending of $J = 26$, outlined in Figure 14, is clearly visualized in the GPT diagram.

Figure 15 shows the evolution of angular momentum using GPT. The emergence of two Back Bendings at $J = 12$ and $J = 26$ can be clearly observed, including the GPT corresponding to the experimental and theoretical data under the assumption of the rigid rotator.

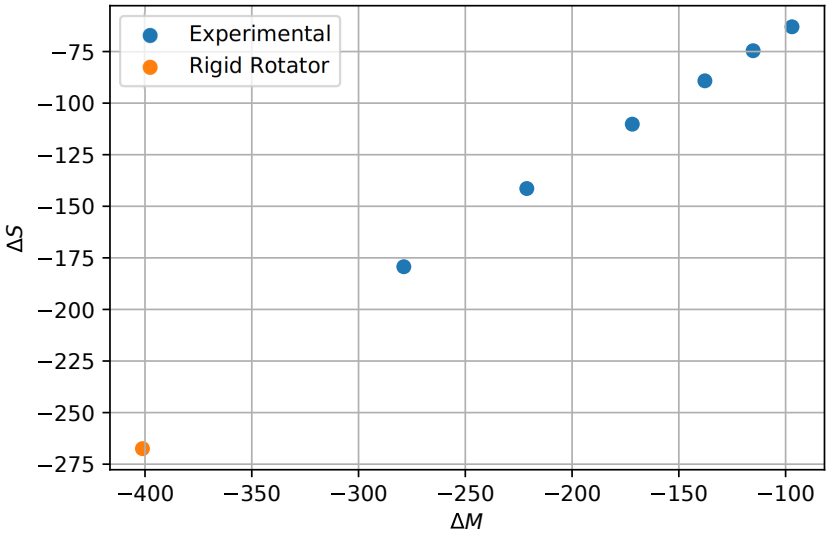

Figure 13. Evolution of angular momentum at ^{170}Hf using GPT and comparison of experimental (blue dots) and theoretical values (orange dot).

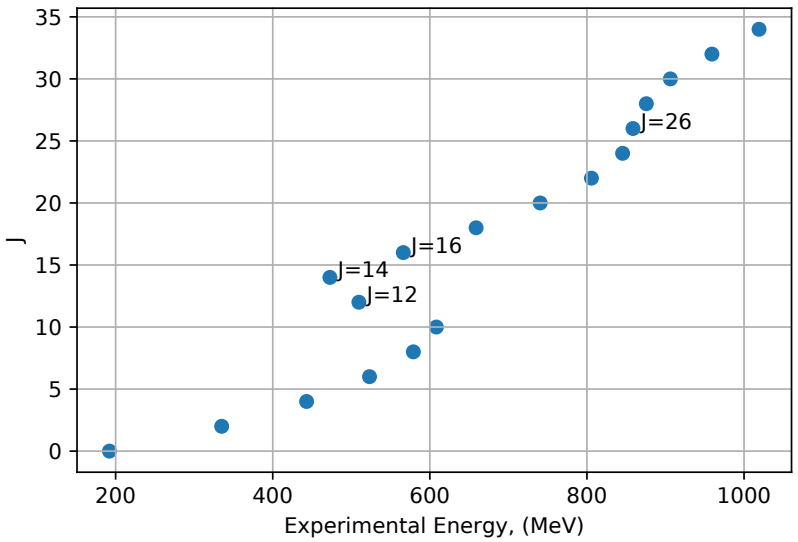

Figure 14. Back Bending of the ^{158}Er using theoretical values for the energy levels.

Finally, the rotational behaviour of the four-nucleus cascades showing Back Bending can be seen in the GPT plot, in Figure 16. It is noteworthy that the evolution of all of them is concentrated in a kind of attractor that points towards the theoretical states of a rigid rotator.

The proposed GPT tool allows the detection of an experimental quantum cascade and its relationship with the theoretically expected evolution which, in the cases analyzed, consists of a single point. It should be noted that GPT can be applied to a signal that consists of only a few data points. That it cannot be increased by expanding the sampling frequency and due to the length of the data series limited by the nature of the experimental quantity of excited states.

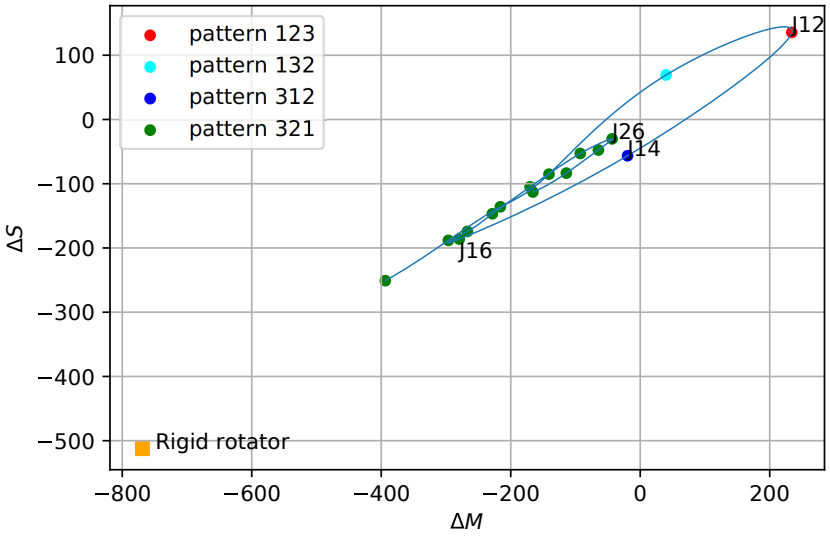

Figure 15. Evolution of angular momentum at ^{158}Er using GPT. The solid line is for tracking the order of data points increasing the quantum number J. In addition, the theoretical value is displayed (square).

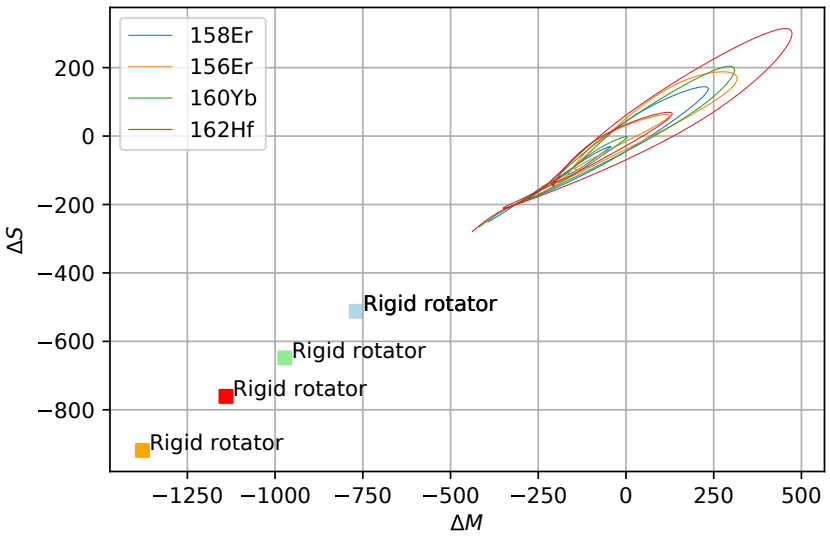

Figure 16. GPT for four nucleus, enclosed in ovals, are the points belonging to Back Bending and the squares correspond to the theoretical rigid rotation. The solid lines are shown in order so as to visualize the location of the GTP data points.

6. Entropic measure from the GPT

To compute a quantitative measure that can distinguish among different types of signals as well as distinct kinds of function increasing, the following methodology is proposed. After applying the GPT to a signal, for every point (δ_M, δ_S) in the $\Delta M \times \Delta S$ plane their polar coordinates (r, θ) are considered. From Figure 3b, the angles

$\alpha_1 = \arccos(2\sqrt{5}/5)$, $\alpha_2 = \arccos(3\sqrt{10}/10)$ and $\alpha_3 = 3\pi/4$ are used to assign a pattern according to the rule:

$$\text{pattern}(\delta_M, \delta_S) = \text{pattern}(r, \theta) = \begin{cases} \text{pattern } 213 & \text{if } 0 \leq \theta < \theta_1, \\ \text{pattern } 123 & \text{if } \theta_1 \leq \theta < \theta_2, \\ \text{pattern } 132 & \text{if } \theta_2 \leq \theta < \theta_3, \\ \text{pattern } 231 & \text{if } \theta_3 \leq \theta < \theta_4, \\ \text{pattern } 321 & \text{if } \theta_4 \leq \theta < \theta_5, \\ \text{pattern } 312 & \text{if } \theta_5 \leq \theta < 2\pi, \end{cases} \tag{19}$$

where $\theta_1 = \alpha_1$, $\theta_2 = \theta_1 + \alpha_2$, $\theta_3 = \theta_2 + \alpha_3$, $\theta_4 = \theta_3 + \alpha_1$ and $\theta_5 = \theta_4 + \alpha_2$.

Given an interval $I = [a, b] \subset \mathbb{R}$ and a positive integer $\mathcal{N}$, the $\mathcal{N}$-partition of I is defined as

$$\pi_{\mathcal{N}}(I) = \bigcup_{i=0}^{\mathcal{N}-1} A_i, \tag{20}$$

where $A_0 = [a, a + \mathcal{L}]$ and $A_i = (a + i\mathcal{L}, a + (i + 1)\mathcal{L}]$ for $i = 1, \ldots, \mathcal{N} - 1$ provided that $\mathcal{L} = (b - a)/\mathcal{N}$.

Let $D = \{\|(\delta_M, \delta_S)\|/(\delta_M, \delta_S) \in \Delta M \times \Delta S\}$ where $\|\cdot\|$ denotes the euclidean 2-norm. The $\mathcal{N}$-partition of the interval $I = [\min(D), \max(D)]$ is built with

$$\mathcal{N} = \max\{\mathcal{M} \in \mathbb{Z}^+ / \forall A \text{ interval in } \pi_{\mathcal{M}}(I) : A \cap D \neq \emptyset\}. \tag{21}$$

It is worth noticing that the elements in D represent the distance between the points obtained by the GPT and the coordinate origin in the $\Delta M \times \Delta S$ plane. Given a pattern ρ, the sets $T_\rho = \{(\delta_M, \delta_S) \in \Delta M \times \Delta S / \text{pattern}(\delta_M, \delta_S) = \rho\}$ and $D_\rho = \{\|(\delta_M, \delta_S)\|/(\delta_M, \delta_S) \in T_\rho\}$ are defined. Thus, a probability density function is defined as follows

$$p_i = \frac{\text{amount of elements in } D_\rho \cap A_i}{\text{amount of elements in } D_\rho}, \tag{22}$$

for $i = 0, \ldots, \mathcal{N} - 1$. The normalized entropy of the pattern ρ is then computed by

$$H_\rho = \frac{1}{\ln(\mathcal{N})} \sum_{i=0}^{\mathcal{N}-1} p_i \ln(p_i). \tag{23}$$

Finally, a vector of entropy for a signal is obtained by

$$\overrightarrow{H} = (H_{213}, H_{123}, H_{132}, H_{231}, H_{321}, H_{312}). \tag{24}$$

The case of an empty pattern counting is denoted by the symbol $\oslash$ in the corresponding coordinate of $\overrightarrow{H}$.

Table 3 shows the results of $\overrightarrow{H}$ for well known synthetic signals, where each components is the mean of 100 independent trials. It can be seen that for the polynomial functions two options for this vector are possible. This property is explained as follows. It is clear that β is a root of the considered functions of this type. Assume β_l and β_r in the domain of the time series are such that β_l is the maximum value that satisfies the condition $x < \beta$ and β_r is the minimum value verifying $x > \beta$. Thus, if $f(\beta_l) < f(\beta_r)$,the null component in $\overrightarrow{H}$ is H_{213}; otherwise it is H_{312}. With the aim to compare the results obtained using the present proposal with a classical methodology, the Bandt and Pompe permutation entropy was also computed using an embedding dimension equal to 3 and 1 as the embedding time delay.

In order to illustrate the behavior of the vector of entropy in terms of the length of the signal, the functions $f_1(x) = e^x$, $f_2(x) = \ln(x)$ and $f_3(x) = x^{-1}$ are considered in the domain $[1, 10]$. It is straightforward that five components in $\overrightarrow{H}$ are empty, except for H_{123} for f_1 and f_2, and H_{321} for f_3, which are positive. Figure 17 shows that there exists a tendency of these values to stabilize as the length of the signal grows.

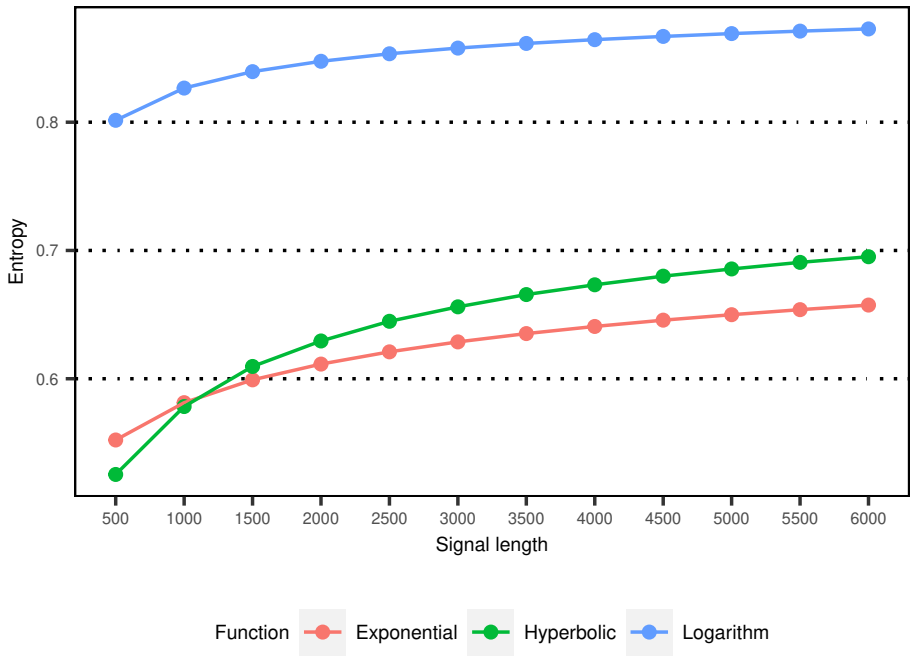

Figure 17. Tendency of the non-empty and non-zero component of the vector of entropy in terms of signal length.

Table 3. Average Bandt and Pompe entropy (BP) and vector of entropy for well known continuous functions with domain $[1, 10]$, where $\alpha > 0$, $1 < \beta < \gamma < 10$, $1 \leq \delta \leq 2$, $2 \leq \varepsilon \leq 10$ and $2 \leq \zeta \leq 3$.

Function	**BP**	H_{213}	H_{123}	H_{132}	H_{231}	H_{321}	H_{312}
$f(x) = \alpha x$	0.00	⊘	0.00	⊘	⊘	⊘	⊘
$f(x) = -\alpha x$	0.00	⊘	⊘	⊘	⊘	0.00	⊘
$f(x) = (x-\beta)^2$	0.36	0.00 ⊘	0.92 0.92	⊘ ⊘	⊘ ⊘	0.99 0.96	⊘ 0.00
$f(x) = (x-\beta)x^2$	0.27	0.00 ⊘	0.98 0.98	⊘ ⊘	⊘ ⊘	0.50 0.68	⊘ 0.00
$f(x) = x(x-\beta)(x-\gamma)$	0.37	0.00 ⊘	0.98 0.98	⊘ 0.00	0.00 ⊘	0.76 0.63	⊘ 0.00
$f(x) = x^{-\delta}$	0.00	⊘	⊘	⊘	⊘	0.53	⊘
$f(x) = \log_{\varepsilon}(x)$	0.00	⊘	0.87	⊘	⊘	⊘	⊘
$f(x) = \zeta^{x}$	0.00	⊘	0.68	⊘	⊘	⊘	⊘

The comparison of the results of the vector of entropy when applied to different types of noises involves the study of white noise distributed uniformly in the interval $[0, 1]$ and coloured noises -gaussian white, red, violet- with $\mu = 0$ and $\sigma = 1$. The mean values of 100 trials are shown in Figure 18. These means allow us to determine that for all the considered cases, the values of H_{132} and H_{312} are lower than the other four components. The uniform white noise shows a notorious higher entropy compared to the coloured noises. The deviation is 0.0183 for the uniform white noise and nearly four times larger for the rest of the noises. It is evident that none of the components of the vector

of entropy vanishes for coloured noises. However, it appears to be a tendency that may allow us to distinguish among them. The valleys located at the patterns 132 and 312 can be explained by the distribution of the GPT points in the hexagon and the way in which the vector of entropy is computed since it distinguishes the distance between the points and the origin of coordinates instead of their position the plane. In other words, many of the GPT points in the corresponding triangles are concentrated in a few numbers of concentric rings which produce a low value of entropy. The opposite case arises for the triangles occupied by the patterns 123 and 321 for which the entropy presents peaks. Another interesting remark is that the entropy is symmetric for the patterns opposite to the vertex (see Figure 7), which may be caused since the same number of pieces in the partition covers the same area of these pairs of triangles, as well as the point clouds in every triangle have a similar dispersion. This property can also be appreciated in Figure 19 that shows the densities of the components of $\overrightarrow{H}$ for the considered noises. The case of uniform white noise is clearly identified since all the entropy components achieve the largest values in the six components. Moreover, it can be noticed that red noise is characterized by smaller values in components H_{123} and H_{321}. On the other side, gaussian white and violet noises can be distinguished since the last ones show a significant greater value in components H_{132} and H_{231}.

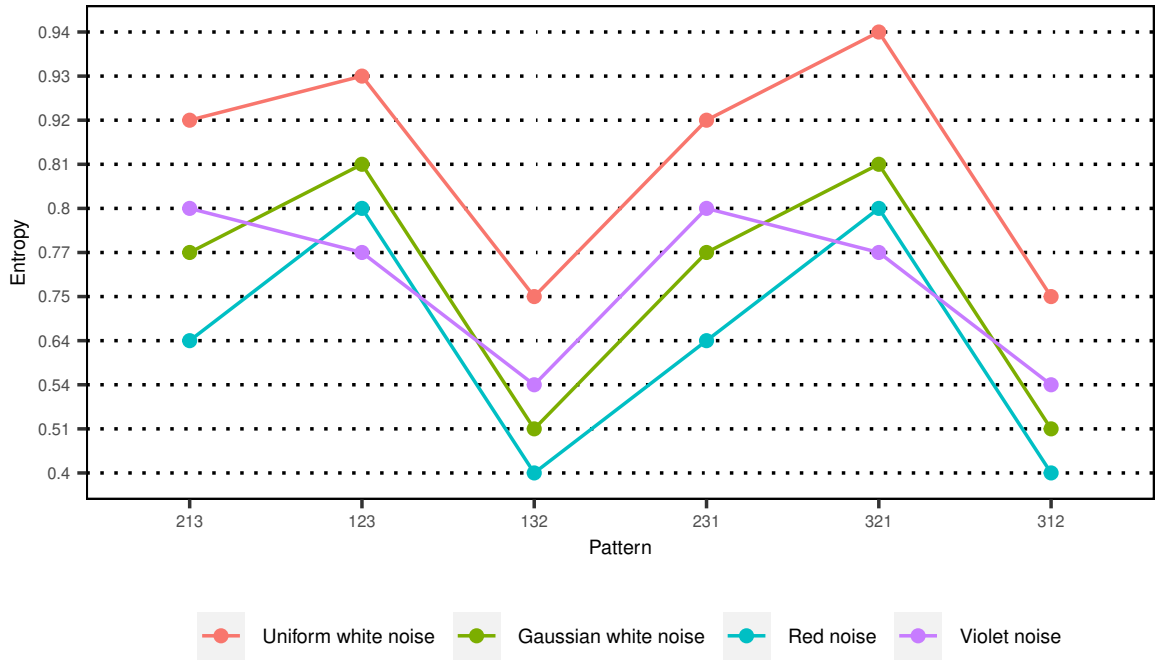

Figure 18. Mean of vector of entropy for different types of noise.

To check the values obtained with the vector of entropy proposed in the present work, this vector was calculated on two well established examples, the Chua oscillator [10] and the Rössler oscillator [19] for the usual parameters values, in such a way to ensure the chaotic behaviour. Table 4 shows the results for the three variables of each oscillator. In the first column, the Bandt and Pompe entropy was calculated, using the previously defined parameters. It can be easily observed that, for each variable, the powerful Bandt and Pompe methodology gives an expected value for the signals of each chaotic system, which are practically the same entropy value, while the values in the vector of entropy differentiate both oscillators clearly. The last row of Table 4 exhibits the values in the logistic equation for the parameter settled to 4, where the differences with the two other chaotic systems considered can be appreciated.

The experiments were developed in a computer with processor Intel© Core™, i7-6700K CPU 3.40 GHz, 16 GB RAM, System Type 64-bit operating system. Figure 20 shows the elapsed time (in seconds) consumed in the

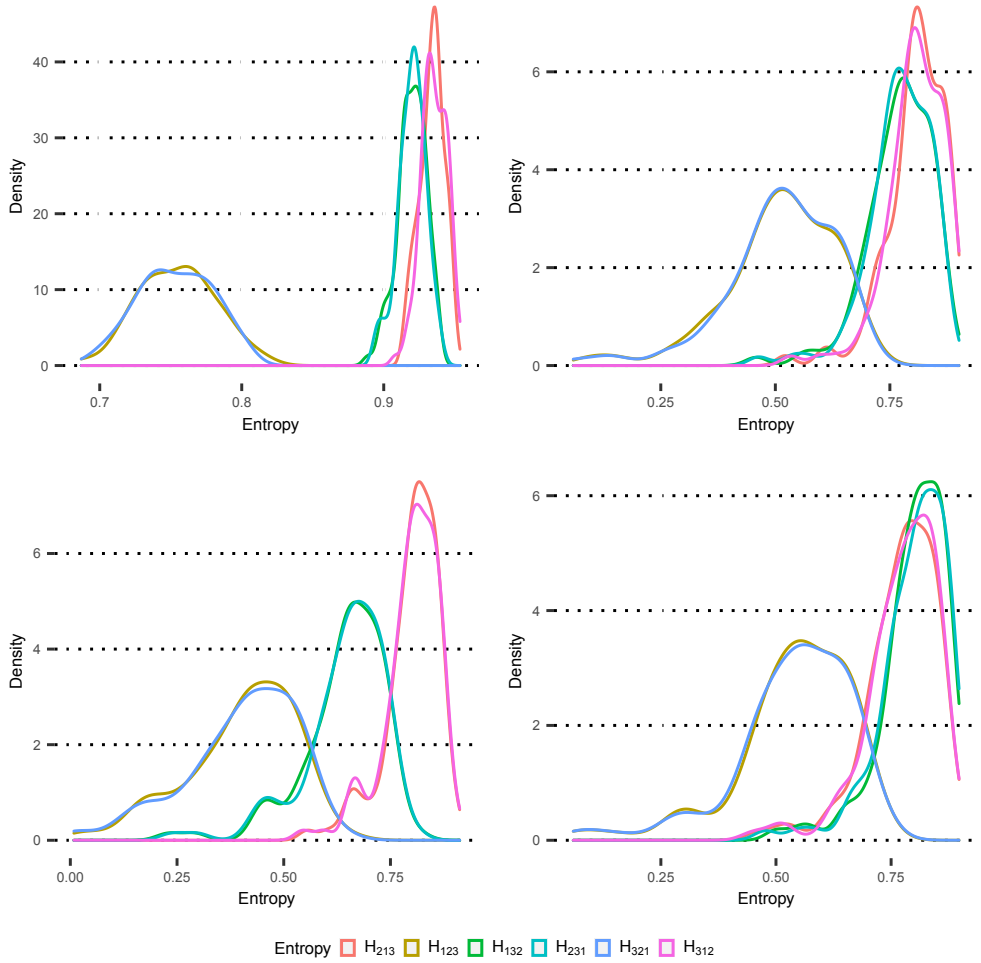

Figure 19. Vector of entropy components density for uniform white noise (top left), gaussian white noise (top right), red noise (bottom left) and violet noise (bottom right).

Table 4. Bandt and Pompe entropy and vector of entropy for different chaotic signals.

Signal	**BP**	H_{213}	H_{123}	H_{132}	H_{231}	H_{321}	H_{312}
Chua x	0.49	0.23	0.93	0.11	0.23	0.92	0.03
Chua y	0.50	0.49	0.95	0.40	0.47	0.95	0.41
Chua z	0.50	0.21	0.92	0.10	0.22	0.92	0.08
Rössler x	0.40	0.00	0.95	0.00	0.12	0.80	0.00
Rössler y	0.42	0.25	0.90	0.00	0.00	0.90	0.13
Rössler z	0.42	0.00	0.43	0.14	0.13	0.39	0.00
Logistic	0.85	0.63	0.68	0.53	0.89	⊘	0.38

vector of entropy computation for different signal lengths. Meanwhile, these times almost vanish for the Bandt and Pompe methodology. It can be seen that they increase for long series when our proposal is applied. However, the computational cost is no extremely expensive compared with the stronger differentiation that can be obtained.

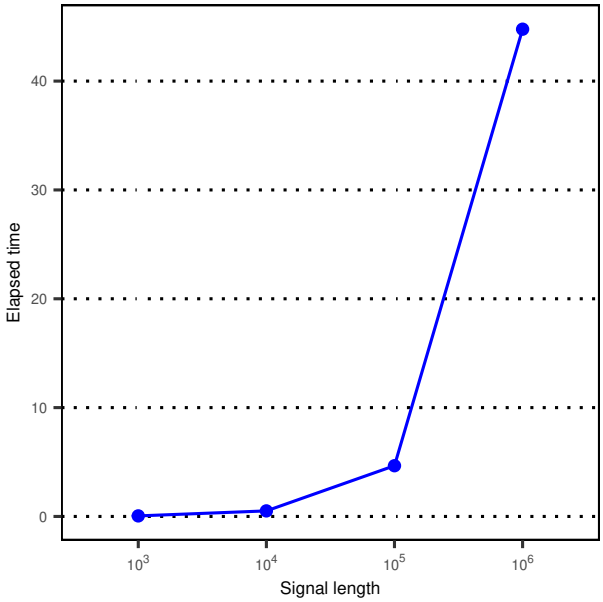

Figure 20. Elapsed time (in seconds) consumed to compute the vector of entropy.

7. Conclusions

The present work develops two perspectives, one focused on the introduction of a Geometric Pattern Transformation and the other one concerned with the definition of a vector of entropy based on this GPT.

It is worth mentioning that in the application of this proposal it is not necessary to make any assumption about the nature of the signal or the statistical distribution of its data points. In this sense, one of the most significant facts of the present GPT for the computation of signal entropy is that it does not require the adjustment of any parameter.

The GPT can be applied to very short data series as was indicated in the example of the Back Bending quantum reaction in Section 5. The new methodology has the capability to differentiate structural signal characteristics belonging to similar patterns. The problem of the missing or forbidden patterns does not appear in the use of the GPT due to the fact that the proposed approach takes into account only the true points constituting the signal. The simplicity of the GPT algorithm is efficient in computational terms in such a way that it can be implemented in real time signal analysis.

Some of the interesting features of the vector of entropy are listed as follows: *i*) The computation of the signal entropy from the GPT contributes to differentiate chaotic from random signals under analysis. *ii*) The construction of a vector of entropy associated with the signal patterns allows us to describe the main characteristics of the signal shape in a compact way. *iii*) Entropy computation is based upon strictly geometric features of the signal, in such a way that it does not require any assumption about the signal nature nor other characteristics of the dynamics process.

Further lines of research can include the exploration of the alternatives of patterns counting algorithms, the incorporation of sub patterns to do a fine tuning of entropy computation, and other variants to segment every region generated by the GPT.

Supplementary material

For reproducibility the code implemented in this work is available at https://arey1911.github.io/GPT/Tutorial.html.

Acknowledgments

We are very grateful to Mario Mariscotti for his helpful comments regarding the Back Bending process. This research was supported by the Universidad Tecnolgica Nacional Grant PID 8120.

REFERENCES

1. Saddon T Ahmad, M Kotb, Idris H Salih, and Hewa Y Abdullah. Backbending phenomena in even–even $^{162-172}$ Hf isotopes. *Physics of Atomic Nuclei*, 84(1):18–28, 2021.
2. TV Alenicheva, P Kabina, IA Mitropolsky, and TM Tyukavina. Iaea nuclear data section. *Wagramer strasse5, A-1400 Viena, INDC (CCP)*, page 439, 2004.
3. José Amigó. *Permutation complexity in dynamical systems: ordinal patterns, permutation entropy and all that*. Springer Science & Business Media, 2010.
4. Christoph Bandt and Bernd Pompe. Permutation entropy: a natural complexity measure for time series. *Physical Review Letters*, 88(17):174102, 2002.
5. George Bergman. A number system with an irrational base. *Mathematics Magazine*, 31(2):98–110, 1957.
6. R Budaca and AA Raduta. Semi-microscopic description of the double backbending in some deformed even–even rare earth nuclei. *Journal of Physics G: Nuclear and Particle Physics*, 40(2):025109, 2013.
7. Inmaculada Leyva Callejas, Johann Martinez, Cristina Masoller, Osvaldo A Rosso, and Massimiliano Zanin. 20 years of ordinal patterns: Perspectives and challenges. *Europhysics Letters*, 2022.
8. Isadora Cardoso-Pereira, João B Borges, Pedro H Barros, Antonio F Loureiro, Osvaldo A Rosso, and Heitor S Ramos. Leveraging the self-transition probability of ordinal patterns transition network for transportation mode identification based on gps data. *Nonlinear Dynamics*, 107(1):889–908, 2022.
9. Zhe Chen, Yaan Li, Hongtao Liang, and Jing Yu. Improved permutation entropy for measuring complexity of time series under noisy condition. *Complexity*, 2019, 2019.
10. Leon O. Chua. A glimpse of nonlinear phenomena from Chua's oscillator. *Philosophical Transactions of the Royal Society of London. Series A: Physical and Engineering Sciences*, 353(1701):3–12, 1995.
11. David Cuesta-Frau. Using the information provided by forbidden ordinal patterns in permutation entropy to reinforce time series discrimination capabilities. *Entropy*, 22(5):494, 2020.
12. R Mà Diamond, FS Stephens, and WJ Swiatecki. Centrifugal stretching of nuclei. *Physics Letters*, 2(4), 1964.
13. Hans Frauenfelder and Ernest M. Henley. *Subatomic physics*. Prentice-Hall, Inc., Englewood Cliffs, NJ, 1974.
14. Karsten Keller. Entropy measures for data analysis: Theory, algorithms and applications, 2019.
15. Douglas Lind and Brian Marcus. *An introduction to symbolic dynamics and coding*. Cambridge university press, 2021.
16. Douglas J Little and Deb M Kane. Variance of permutation entropy and the influence of ordinal pattern selection. *Physical Review E*, 95(5):052126, 2017.
17. Mo Ao J Mariscotti, Gertrude Scharff-Goldhaber, and Brian Buck. Phenomenological analysis of ground-state bands in even-even nuclei. *Physical Review*, 178(4):1864, 1969.
18. Lederer C. Michael, Virginia S. Shirley, et al. *Table of Isotopes*. John Wiley & Sons, 1978.
19. Otto E. Rössler. The chaotic hierarchy. *Zeitschrift für Naturforschung A*, 38(7):788–801, 1983.
20. Osvaldo A. Rosso and Cristina Masoller. Detecting and quantifying temporal correlations in stochastic resonance via information theory measures. *The European Physical Journal B*, 69(1):37–43, 2009.
21. Osvaldo A. Rosso, Felipe Olivares, Luciano Zunino, Luciana De Micco, André L. Aquino, Angelo Plastino, and Hilda A. Larrondo. Characterization of chaotic maps using the permutation Bandt-Pompe probability distribution. *The European Physical Journal B*, 86(4):1–13, 2013.
22. Hans Ryde. Chronicle of the discovery of the back-bending phenomenon in atomic nuclei: a personal recollection 50 years on. *The European Physical Journal H*, 46(1):1–5, 2021.
23. Alexey Stakhov. The importance of the golden number for mathematics and computer science: Exploration of the Bergmans system and the Stakhov's ternary mirror-symmetrical system (numeral systems with irrational bases). *Journal of Advances in Mathematics and Computer Science*, 18(3):1–34, 2016.
24. Sudharsan Thiruvengadam, Jei Shian Tan, and Karol Miller. Time series, hidden variables and spatio-temporal ordinality networks. *Advances in Applied Clifford Algebras*, 30(3):1–98, 2020.
25. Francisco Traversaro, Francisco O. Redelico, Marcelo R. Risk, Alejandro C. Frery, and Osvaldo A. Rosso. Bandt-Pompe symbolization dynamics for time series with tied values: A data-driven approach. *Chaos: An Interdisciplinary Journal of Nonlinear Science*, 28(7):075502–1–14, 2018.
26. Valentina A. Unakafova and Karsten Keller. Efficiently measuring complexity on the basis of real-world data. *Entropy*, 15(10):4392–4415, 2013.

27. Massimiliano Zanin, Luciano Zunino, Osvaldo A. Rosso, and David Papo. Permutation entropy and its main biomedical and econophysics applications: a review. *Entropy*, 14(8):1553–1577, 2012.
28. Hristo Zhivomirov. A method for colored noise generation. *Romanian Journal of Acoustics and Vibration*, 15(1):14–19, 2018.